Magnon Polarons in the Spin Seebeck Effect

Takashi Kikkawa, Ka Shen, Benedetta Flebus, Rembert A. Duine, Ken-ichi Uchida, Zhiyong Qiu, Gerrit E. W. Bauer, and Eiji Saitoh

Phys. Rev. Lett. **117**, 207203 — Published 10 November 2016

DOI: 10.1103/PhysRevLett.117.207203

Magnon-Polarons in the Spin Seebeck Effect

Takashi Kikkawa,[1,2,*] Ka Shen,[3] Benedetta Flebus,[4] Rembert A. Duine,[4,5] Ken-ichi Uchida,[1,6,7,†] Zhiyong Qiu,[2,8] Gerrit E. W. Bauer,[1,2,3,7] and Eiji Saitoh[1,2,7,8,9]

[1]*Institute for Materials Research, Tohoku University, Sendai 980-8577, Japan*

[2]*WPI Advanced Institute for Materials Research, Tohoku University, Sendai 980-8577, Japan*

[3]*Kavli Institute of NanoScience, Delft University of Technology, Lorentzweg 1, 2628 CJ Delft, The Netherlands*

[4]*Institute for Theoretical Physics and Center for Extreme Matter and Emergent Phenomena, Utrecht University, Leuvenlaan 4, 3584 CE Utrecht, The Netherlands*

[5]*Department of Applied Physics, Eindhoven University of Technology, PO Box 513, 5600 MB Eindhoven, The Netherlands*

[6]*PRESTO, Japan Science and Technology Agency, Saitama 332-0012, Japan*

[7]*Center for Spintronics Research Network, Tohoku University, Sendai 980-8577, Japan*

[8]*Spin Quantum Rectification Project, ERATO, Japan Science and Technology Agency, Sendai 980-8577, Japan*

[9]*Advanced Science Research Center, Japan Atomic Energy Agency, Tokai 319-1195, Japan*

(Dated: September 30, 2016)

Abstract

Sharp structures in magnetic field-dependent spin Seebeck effect (SSE) voltages of Pt/$Y_3Fe_5O_{12}$ (YIG) at low temperatures are attributed to the magnon-phonon interaction. Experimental results are well reproduced by a Boltzmann theory that includes the magnetoelastic coupling (MEC). The SSE anomalies coincide with magnetic fields tuned to the threshold of magnon-polaron formation. The effect gives insight into the relative quality of the lattice and magnetization dynamics.

PACS numbers: 85.75.-d, 72.25.-b, 75.80.+q, 72.25.Mk

The spin Seebeck effect (SSE) [1–19] refers to the generation of a spin current ($\mathbf{J}^s$) as a result of a temperature gradient (∇T) in magnetic materials. It is well established for magnetic insulators with metallic contacts, at which a magnon flow is converted into a conduction-electron spin current by the interfacial exchange interaction [20] and detected as a transverse electric voltage via the inverse spin Hall effect (ISHE) [21–27] [see Fig. 1(a)]. The SSE provides a sensitive probe for spin correlations in magnetic materials [8, 9, 12–15].

The ferrimagnetic insulator yttrium-iron-garnet $Y_3Fe_5O_{12}$ (YIG) is ideal for SSE measurements [19], exhibiting a long magnon-propagation length [28–30], high Curie temperature (~ 560 K) [31], and high resistivity owing to a large band gap (~ 2.9 eV) [32]. The magnon and phonon dispersion relations in YIG are well known [33–38]. The magnon dispersion in the relevant regime reads

$$\omega_{\mathbf{k}} = \sqrt{D_{\mathrm{ex}}k^2 + \gamma\mu_0 H}\sqrt{D_{\mathrm{ex}}k^2 + \gamma\mu_0 H + \gamma\mu_0 M_{\mathrm{s}}\sin^2\theta}, \tag{1}$$

where ω, $\mathbf{k}$, θ, γ, $\mu_0 M_{\mathrm{s}}$, are the angular frequency, wave vector $\mathbf{k}$ with length k, angle θ with the external magnetic field $\mathbf{H}$ (of magnitude H), gyromagnetic ratio, and saturation magnetization, respectively [33–36]. The exchange stiffness coefficient D_{ex} as well as transverse-acoustic (TA) and longitudinal-acoustic (LA) sound velocities for YIG are summarized in Table I and the dispersion relations are plotted in Fig. 1(b).

In this Letter, we report the observation of a resonant enhancement of the SSE. The experimental results are well reproduced by a theory for the thermally induced magnon flow in which the magnetoelastic interaction is taken into account. We interpret the experiments as evidence for a strong magnon-phonon coupling at the crossings between the magnon and phonon dispersion curves, i.e., the formation of hybridized excitations called magnon-polarons [40, 41].

The sample is a 5-nm-thick Pt film sputtered on the (111) surface of a 4-μm-thick single-crystalline YIG film grown on a single-crystalline $Gd_3Ga_5O_{12}$ (GGG) (111) substrate by liquid phase epitaxy [42]. The sample was then cut into a rectangular shape with $L_V =$ 4.0 mm (length), $L_W = 2.0$ mm (width), and $L_T = 0.5$ mm (thickness). SSE measurements were carried out in a longitudinal configuration [1, 19] [see Fig. 1(a)], where the temperature gradient ∇T is applied normal to the interfaces by sandwiching the sample between two sapphire plates, on top of the Pt layer (at the bottom of the GGG substrate) stabilized to $T_{\rm H}$ ($T_{\rm L}$) with temperature difference $\Delta T = T_{\rm H} - T_{\rm L}$ (> 0). ΔT was measured with two calibrated Cernox thermometers. A uniform magnetic field $\mathbf{H} = H\hat{\mathbf{z}}$ was applied by a superconducting solenoid magnet. We measured the DC electric voltage difference V between the ends of the Pt layer with a highly resolved field scan, i.e., at intervals of 15 mT and waiting for $\sim$ 30 sec after each step.

Figure 2(b) shows the measured $V(H)$ of the Pt/YIG sample at $T = 50$ K. A clear signal appears by applying the temperature difference ΔT and its sign is reversed when reversing the magnetization. The magnitude of V at $\mu_0 H = 0.1$ T is proportional to ΔT [see Fig. 2(c)]. These results confirm that V is generated by the SSE [19].

Owing to the high resolution of H, we were able to resolve a fine peak structure at $\mu_0 H \sim 2.6$ T that is fully reproducible. A magnified view of the V-H curve is shown in Fig. 2(d), where the anomaly is marked by a blue triangle. Since the structures scale with ΔT [see Figs. 2(c) and 2(d)], they must stem from the SSE.

The peak appears for the field $H_{\rm TA}$ at which according to the parameters in Table I the magnon dispersion curve touches the TA-phonon dispersion curve. By increasing H, the magnon dispersion shifts toward high frequencies due to the Zeeman interaction ($\propto \gamma\mu_0 H$), while the phonon dispersion does not move. At $\mu_0 H = 0$, the magnon branch intersects the TA-phonon curve twice [see Fig. 2(a)]. With increasing H, TA-phonon branch becomes tangential to the magnon dispersion at $\mu_0 H = 2.6$ T and detaches at higher fields [see Fig. 2(a)]. If the anomaly is indeed linked to the "touch" condition, there should be another peak associated to the LA-phonon branch. Based on the parameters in Table I, we evaluated the magnon−LA-phonon touch condition at $\mu_0 H_{\rm LA} \sim 9.3$ T. We then upgraded the equipment with a stronger magnet and subsequently investigated the high-field dependence of the SSE.

Figure 2(f) shows the dependence $V(H)$ of the Pt/YIG sample at $T = 50$ K, measured between $\mu_0 H = \pm 10.5$ T. Indeed, another peak appeared at $\mu_0 H_{\rm LA} \sim 9.3$ T precisely at the estimated field value at which the LA-phonon branch touches the magnon dispersion [see Fig. 2(e)], sharing the characteristic features of the SSE, i.e., it appears only when $\Delta T \neq 0$ and exhibits a linear-ΔT dependence [see Figs. 2(g) and 2(h)]. For $\mu_0 H > 9.3$ T the V-H curves remain smooth.

We carried out systematic measurements of the temperature dependence of the SSE enhancement at $H_{\rm TA}$ and $H_{\rm LA}$. Figure 3(c) shows the normalized SSE voltage $S \equiv (V/\Delta T)(L_T/L_V)$ as a function of H for various average sample temperature $T_{\rm avg}$ [$\equiv$

$(T_\mathrm{H} + T_\mathrm{L})/2]$. The amplitude of the SSE signal monotonically decreases with decreasing T in the present temperature range [8, 9] [see Fig. 3(b)]. Importantly, the two peaks in S at H_TA and H_LA exhibit different T dependences [see Figs. 3(c), 3(d), and 3(e)]. The peak shape at H_TA becomes more prominent with decreasing T and it is the most outstanding at the lowest T. On the other hand, the S peak at H_LA is suppressed below ~ 10 K and it is almost indistinguishable at the lowest T. This different T dependence can be attributed to the different energy scale of the branch crossing point for $H = H_\mathrm{TA}$ and $H = H_\mathrm{LA}$. The frequency of the magnon−LA-phonon intersection point is 0.53 THz = 26 K ($\equiv T_\mathrm{MLA}$), and it is more than three times larger than that of the magnon−TA-phonon intersection point (0.16 THz). Therefore, for $T < T_\mathrm{MLA}$, excitation of magnons with energy around the magnon−LA-phonon intersection point is rapidly suppressed which leads to the disappearance of the S peak at H_LA at the lowest T.

The clear peak structures at low temperatures allow us to unravel the behavior of the SSE around H_TA in detail. Increasing H from small values, S increases up to a maximum value at $H = H_\mathrm{TA}$, as shown in Fig. 3(d) ($T_\mathrm{avg} = 3.46$ K). For fields slightly larger than H_TA, S drops steeply to a value below the initial one. The SSE intensity $S(i)$, where i $(= 0, 1, 2)$ represents the number of crossing points between the magnon and (TA-)phonon branch curves [see also Fig. 2(a)], can be ordered as $S(1) > S(2) > S(0)$ and could be a measure of the number of magnon-polarons.

The SSE is generated in three steps: (i) the temperature gradient excites magnetization dynamics that (ii) at the interface to the metal becomes a particle spin current and (iii) is converted to a transverse voltage by the ISHE. The latter two steps depend only weakly on the magnetic field. For thick enough samples, the observed anomalies in the SSE originate from the thermally excited spin current in the bulk of the ferromagnet. The importance of the magnetoelastic coupling (MEC) for spin transport in magnetic insulators has been established by spatiotemporally resolved pump-and-probe optical spectroscopy [41, 43]. Here we develop a semiclassical model for the SSE in the strongly coupled magnon-phonon transport regime [40, 41, 44–46]. Our model Hamiltonian consists of magnon ($\mathcal{H}_\mathrm{mag}$), phonon ($\mathcal{H}_\mathrm{el}$), and magnetoelastic coupling ($\mathcal{H}_\mathrm{mec}$) terms. In second-quantized form $\mathcal{H}_\mathrm{mag} = \sum_\mathbf{k} A_\mathbf{k} a^\dagger_\mathbf{k} a_\mathbf{k} + (B_\mathbf{k}/2)(a^\dagger_\mathbf{k} a^\dagger_{-\mathbf{k}} + a_{-\mathbf{k}} a_\mathbf{k})$, $\mathcal{H}_\mathrm{el} = \sum_{\mathbf{k},\mu} \hbar\omega_{\mu\mathbf{k}} \left(c^\dagger_{\mu\mathbf{k}} c_{\mu\mathbf{k}} + \frac{1}{2} \right)$, and $\mathcal{H}_\mathrm{mec} = \hbar n B_\perp (\frac{\gamma\hbar}{4M_s\rho})^{1/2} \sum_{\mathbf{k},\mu} k \omega^{-1/2}_{\mathbf{k}\mu} e^{-i\phi} a_\mathbf{k} (c_{\mu-\mathbf{k}} + c^\dagger_{\mu\mathbf{k}}) \times (-i\delta_{\mu 1} \cos 2\theta + i\delta_{\mu 2} \cos\theta - \delta_{\mu 3} \sin 2\theta) + h.c.$. In spherical coordinates the wave vector $\mathbf{k} = k(\sin\theta\cos\phi, \sin\theta\sin\phi, \cos\theta)$,

$A_{\mathbf{k}}/\hbar = D_{\rm ex}k^2 + \gamma\mu_0 H + (\gamma\mu_0 M_{\rm s}\sin^2\theta)/2$, and $B_{\mathbf{k}}/\hbar = (\gamma\mu_0 M_{\rm s}\sin^2\theta)/2$. Here, $a^\dagger_{\mathbf{k}}$ ($c^\dagger_{\mu\mathbf{k}}$) and $a_{\mathbf{k}}$ ($c_{\mu\mathbf{k}}$) are magnon (phonon) creation and annihilation operators, respectively. $B_\perp$ is the magnetoelastic coupling constant, ρ the average mass density, $n = 1/a_0^3$ the number density of spins, and a_0 the lattice constant. The magnon dispersion from $\mathcal{H}_{\rm mag}$ is given by Eq. (1), while the phonon dispersions are $\omega_{\mu\mathbf{k}} = c_\mu k$ with $\mu = 1, 2$ for the two transverse modes and $\mu = 3$ for the longitudinal one. $\delta_{\mu i}$ in $\mathcal{H}_{\rm mec}$ represents the Kronecker delta. By diagonalizing $\mathcal{H}_{\rm mag} + \mathcal{H}_{\rm el} + \mathcal{H}_{\rm mec}$ [47], we obtain the dispersion relation of the i-th magnon-polaron branch $\hbar\Omega_{i\mathbf{k}}$ and the corresponding amplitude $|\psi_{i\mathbf{k}}\rangle$. The magnon-polaron dispersions for $\theta = \pi/2$ and $\phi = 0$ are illustrated in Figs. 1(c) and 1(d), with a magnetic field $\mu_0 H = 1.0$ T and $B_\perp/(2\pi) = 1988$ GHz [38].

We assume diffuse transport that at low temperatures is limited by elastic magnon and phonon impurity scattering [45]. We employ the Hamiltonian $\mathcal{H}_{\rm imp} = \sum_\mu \sum_{\mathbf{k},\mathbf{k}'} c^\dagger_{\mu\mathbf{k}} v^{\rm ph}_{\mathbf{k},\mathbf{k}'} c_{\mu\mathbf{k}'} + \sum_{\mathbf{k},\mathbf{k}'} a^\dagger_{\mathbf{k}} v^{\rm mag}_{\mathbf{k},\mathbf{k}'} a_{\mathbf{k}'}$, where, assuming s-wave scattering, $v^{\rm ph}_{\mathbf{k},\mathbf{k}'} = v^{\rm ph}$ and $v^{\rm mag}_{\mathbf{k},\mathbf{k}'} = v^{\rm mag}$ denote the phonon and magnon impurity scattering potentials, respectively. We compute the spin current driven by a temperature gradient [6, 16] and thereby the SSE in the relaxation-time approximation of the linearized Boltzmann equation. The linear-response steady-state spin current $\mathbf{J}^s(\mathbf{r}) = -\boldsymbol{\zeta}\cdot\nabla T$ is governed by the SSE tensor $\boldsymbol{\zeta}$:

$$\zeta_{\alpha\beta} = \int \frac{d^3\mathbf{k}}{(2\pi)^3} \sum_i W^s_{i\mathbf{k}} \tau_{i\mathbf{k}} (\partial_{k_\alpha}\Omega_{i\mathbf{k}})(\partial_{k_\beta}\Omega_{i\mathbf{k}}) \partial_T f^{(0)}_{i\mathbf{k}}|_{T=T(\mathbf{r})}. \tag{2}$$

Here $W^s_{i\mathbf{k}} = |\langle 0|a_{\mathbf{k}}|\psi_{i\mathbf{k}}\rangle|^2$ is the intensity of the i-th magnon-polaron and $\tau_{i\mathbf{k}}$ is the relaxation time towards the equilibrium (Planck) distribution function $f^{(0)}_{i\mathbf{k}}(\mathbf{r}) = (\exp(\hbar\Omega_{i\mathbf{k}}/(k_{\rm B}T(\mathbf{r}))) - 1)^{-1}$. The relaxation time $\tau_{i\mathbf{k}}$ of the i-th magnon-polaron reads $\tau^{-1}_{i\mathbf{k}} = (2\pi/\hbar)\sum_{j\mathbf{k}'} |\langle\psi_{j\mathbf{k}'}|\mathcal{H}_{\rm imp}|\psi_{i\mathbf{k}}\rangle|^2 \delta(\hbar\Omega_{i\mathbf{k}} - \hbar\Omega_{j\mathbf{k}'})$. The strong-coupling (weak scattering) approach is valid when $\tau^{-1}_{i\mathbf{k}_{1,2}} \ll \Delta\Omega$, where $\Delta\Omega$ is the energy gap at the anti-crossing points $\mathbf{k}_{1,2}$. We disregard the Gilbert damping that is very small in YIG.

From the experiments we infer the scattering parameters $|v^{\rm mag}|^2 = 10^{-5}$ s^{-2} [28] and $\left|v^{\rm mag}/v^{\rm ph}\right| = 10$, i.e., the magnons are stronger scattered than the phonons. The computed longitudinal spin Seebeck coefficient (SSC) ζ_{xx} [Eq. (2)] is plotted in Fig. 4(a). Switching on the magnetoelastic coupling increases the SSC especially at the "touching" magnetic fields $H_{\rm TA}$ and $H_{\rm LA}$. At these points the group velocity of the magnon is identical to the sound velocity. Nevertheless, spin transport can be strongly modified when the ratio $\left|v^{\rm mag}/v^{\rm ph}\right|$

differs from unity. The SSC can be enhanced or suppressed compared to its purely magnonic value. A high acoustic quality as implied by $\left|v^{\mathrm{mag}}/v^{\mathrm{ph}}\right| = 10$ is beneficial for spin transport and enhances the SSC by hybridization, as illustrated by Fig. 4(a). When magnon and phonon scattering potentials would be the same, i.e., $\left|v^{\mathrm{mag}}/v^{\mathrm{ph}}\right| = 1$, the anomalies vanish identically [see blue circles in Fig. 4(a)]. The difference between the calculations with and without MEC agrees very well with the peak features on top of the smooth background as observed in the experiments, see Figs. 4(b) and 4(c). We can rationalize the result by the presence of magnetic disorder that scatters magnons but not phonons.

Finally, we address the SSE background signal. The overall decrease of the calculated ζ_{xx} is not related to the phonons, but reflects the field-induced freeze-out of the magnons (that is suppressed in thin magnetic films [8]). In the experiments, on the other hand, the global S below ~ 30 K clearly increases with increasing H [Fig. 3(c)]. We tentatively attribute this discrepancy to an additional spin current caused by the paramagnetic GGG substrate that, when transmitted through the YIG layer, causes an additional voltage. Wu *et al.* [7] found a paramagnetic SSE signal in a Pt/GGG sample proportional to induced magnetization ($\sim$ a Brillouin function for spin 7/2) [7]. Indeed, the increase of S in the present Pt/YIG/GGG sample is of the same order as the paramagnetic SSE in a Pt/GGG sample [8].

In conclusion, we observed two anomalous peak structures in the magnetic field dependence of the spin Seebeck effect (SSE) in Pt/$Y_3Fe_5O_{12}$ (YIG) that appear at the onset of magnon-polaron formation. The experimental results are well reproduced by a calculation in which magnons and phonons are allowed to hybridize. Our results show that the SSE can probe not only magnon dynamics but also phonon dynamics. The magnitude and shape of the anomalies contain unique information about the sample disorder, depending sensitively on the relative scattering strengths of magnons and phonons.

This work was supported by PRESTO "Phase Interfaces for Highly Efficient Energy Utilization" from JST, Japan, Grant-in-Aid for Scientific Research on Innovative Area "Nano Spin Conversion Science" (No. 26103005, 26103006), Grant-in-Aid for Scientific Research (A) (No. 15H02012, 25247056) and (S) (No. 25220910) from MEXT, Japan, NEC Corporation, The Noguchi Institute, the Dutch FOM Foundation, EU-FET Grant InSpin 612759, and DFG Priority Programme 1538 "Spin-Caloric Transport" (BA 2954/2). T.K. is supported by JSPS through a research fellowship for young scientists (No. 15J08026).

* Electronic address: t.kikkawa@imr.tohoku.ac.jp

† Present address: National Institute for Materials Science, Tsukuba 305-0047, Japan.

[1] K. Uchida, H. Adachi, T. Ota, H. Nakayama, S. Maekawa, and E. Saitoh, Observation of longitudinal spin-Seebeck effect in magnetic insulators, Appl. Phys. Lett. **97**, 172505 (2010).

[2] J. Xiao, G. E. W. Bauer, K. Uchida, E. Saitoh, and S. Maekawa, Theory of magnon-driven spin Seebeck effect, Phys. Rev. B **81**, 214418 (2010).

[3] H. Adachi, J. Ohe, S. Takahashi, and S. Maekawa, Linear-response theory of spin Seebeck effect in ferromagnetic insulators, Phys. Rev. B **83**, 094410 (2011).

[4] S. S.-L. Zhang and S. Zhang, Spin convertance at magnetic interfaces, Phys. Rev. B **86**, 214424 (2012).

[5] S. Hoffman, K. Sato, and Y. Tserkovnyak, Landau-Lifshitz theory of the longitudinal spin Seebeck effect, Phys. Rev. B **88**, 064408 (2013).

[6] S. M. Rezende, R. L. Rodríguez-Suárez, R. O. Cunha, A. R. Rodrigues, F. L. A. Machado, G. A. Fonseca Guerra, J. C. Lopez Ortiz, and A. Azevedo, Magnon spin-current theory for the longitudinal spin-Seebeck effect, Phys. Rev. B **89**, 014416 (2014).

[7] S. M. Wu, J. E. Pearson, and A. Bhattacharya, Paramagnetic spin Seebeck effect, Phys. Rev. Lett. **114**, 186602 (2015).

[8] T. Kikkawa, K. Uchida, S. Daimon, Z. Qiu, Y. Shiomi, and E. Saitoh, Critical suppression of spin Seebeck effect by magnetic fields, Phys. Rev. B **92**, 064413 (2015).

[9] H. Jin, S. R. Boona, Z. Yang, R. C. Myers, and J. P. Heremans, Effect of the magnon dispersion on the longitudinal spin Seebeck effect in yttrium iron garnets, Phys. Rev. B **92**, 054436 (2015).

[10] A. Kehlberger, U. Ritzmann, D. Hinzke, E.-J. Guo, J. Cramer, G. Jakob, M. C. Onbasli, D. H. Kim, C. A. Ross, M. B. Jungfleisch, B. Hillebrands, U. Nowak, and M. Kläui, Length scale of the spin Seebeck effect, Phys. Rev. Lett. **115**, 096602 (2015).

[11] U. Ritzmann, D. Hinzke, A. Kehlberger, E.-J. Guo, M. Kläui, and U. Nowak, Magnetic field control of the spin Seebeck effect, Phys. Rev. B **92**, 174411 (2015).

[12] A. Aqeel, N. Vlietstra, J. A. Heuver, G. E. W. Bauer, B. Noheda, B. J. van Wees, and T. T. M. Palstra, Spin-Hall magnetoresistance and spin Seebeck effect in spin-spiral and paramagnetic

phases of multiferroic $CoCr_2O_4$ films, Phys. Rev. B **92**, 224410 (2015).

[13] S. Seki, T. Ideue, M. Kubota, Y. Kozuka, R. Takagi, M. Nakamura, Y. Kaneko, M. Kawasaki, and Y. Tokura, Thermal generation of spin current in an antiferromagnet, Phys. Rev. Lett. **115**, 266601 (2015).

[14] S. M. Wu, W. Zhang, A. KC, P. Borisov, J. E. Pearson, J. S. Jiang, D. Lederman, A. Hoffmann, and A. Bhattacharya, Antiferromagnetic spin Seebeck effect, Phys. Rev. Lett. **116**, 097204 (2016).

[15] S. Geprägs, A. Kehlberger, F. D. Coletta, Z. Qiu, E.-J. Guo, T. Schulz, C. Mix, S. Meyer, A. Kamra, M. Althammer, H. Huebl, G. Jakob, Y. Ohnuma, H. Adachi, J. Barker, S. Maekawa, G. E. W. Bauer, E. Saitoh, R. Gross, S. T. B. Goennenwein, and M. Kläui, Origin of the spin Seebeck effect in compensated ferrimagnets, Nat. Commun. **7**, 10452 (2016).

[16] S. M. Rezende, R. L. Rodríguez-Suárez, R. O. Cunha, J. C. López Ortiz, and A. Azevedo, Bulk magnon spin current theory for the longitudinal spin Seebeck effect, J. Magn. Magn. Mater. **400**, 171 (2016).

[17] J. Li, Y. Xu, M. Aldosary, C. Tang, Z. Lin, S. Zhang, R. Lake, and J. Shi, Observation of magnon-mediated current drag in Pt/yttrium iron garnet/Pt(Ta) trilayers, Nat. Commun. **7**, 10858 (2016).

[18] E.-J. Guo, J. Cramer, A. Kehlberger, C. A. Ferguson, D. A. MacLaren, G. Jakob, and M. Kläui, Influence of thickness and interface on the low-temperature enhancement of the spin Seebeck effect in YIG films, Phys. Rev. X **6**, 031012 (2016).

[19] K. Uchida, H. Adachi, T. Kikkawa, A. Kirihara, M. Ishida, S. Yorozu, S. Maekawa, and E. Saitoh, Thermoelectric generation based on spin Seebeck effects, Proc. IEEE **104**, 1946 (2016)., *ibid.* **104**, 1499 (2016).

[20] Y. Tserkovnyak, A. Brataas, G. E. W. Bauer, and B. I. Halperin, Nonlocal magnetization dynamics in ferromagnetic heterostructures, Rev. Mod. Phys. **77**, 1375 (2005).

[21] A. Azevedo, L. H. Vilela-Leão, R. L. Rodríguez-Suárez, A. B. Oliveira, and S. M. Rezende, dc effect in ferromagnetic resonance: Evidence of the spin-pumping effect?, J. Appl. Phys. **97**, 10C715 (2005).

[22] E. Saitoh, M. Ueda, H. Miyajima, and G. Tatara, Conversion of spin current into charge current at room temperature: Inverse spin-Hall effect, Appl. Phys. Lett. **88**, 182509 (2006).

[23] S. O. Valenzuela and M. Tinkham, Direct electronic measurement of the spin Hall effect,

Nature **442**, 176 (2006).

[24] M. V. Costache, M. Sladkov, S. M. Watts, C. H. van der Wal, and B. J. van Wees, Electrical detection of spin pumping due to the precessing magnetization of a single ferromagnet, Phys. Rev. Lett. **97**, 216603 (2006).

[25] M. Weiler, H. Huebl, F. S. Goerg, F. D. Czeschka, R. Gross, and S. T. B. Goennenwein, Spin pumping with coherent elastic waves, Phys. Rev. Lett. **108**, 176601 (2012).

[26] L. Bai, M. Harder, Y. P. Chen, X. Fan, J. Q. Xiao, and C.-M. Hu, Spin pumping in electrodynamically coupled magnon-photon systems, Phys. Rev. Lett. **114**, 227201 (2015).

[27] J. Sinova, S. O. Valenzuela, J. Wunderlich, C. H. Back, and T. Jungwirth, Spin Hall effects, Rev. Mod. Phys. **87**, 1213 (2015).

[28] S. R. Boona and J. P. Heremans, Magnon thermal mean free path in yttrium iron garnet, Phys. Rev. B **90**, 064421 (2014).

[29] B. L. Giles, Z. Yang, J. S. Jamison, and R. C. Myers, Long-range pure magnon spin diffusion observed in a nonlocal spin-Seebeck geometry, Phys. Rev. B **92**, 224415 (2015).

[30] L. J. Cornelissen and B. J. van Wees, Magnetic field dependence of the magnon spin diffusion length in the magnetic insulator yttrium iron garnet, Phys. Rev. B **93**, 020403(R) (2016).

[31] M. A. Gilleo and S. Geller, Magnetic and crystallographic properties of substituted yttrium-iron garnet, $3Y_2O_3 \cdot xM_2O_3 \cdot (5-x)Fe_2O_3$, Phys. Rev. **110**, 73 (1958).

[32] R. Metselaar and P. K. Larsen, High-temperature electrical properties of yttrium iron garnet under varying oxygen pressures, Solid State Commun. **15**, 291 (1974).

[33] A. B. Harris, Spin-wave spectra of yttrium and gadolinium iron garnet, Phys. Rev. **132**, 2398 (1963).

[34] F. Keffer, Spin Waves, in *Handbuch der Physik, Vol. XVIII/2: Ferromagnetismus*, edited by H. P. J. Wijn (Springer-Verlag, Berlin Heidelberg, 1966).

[35] C. M. Srivastava and R. Aiyar, Spin wave stiffness constants in some ferrimagnetics, J. Phys. C **20**, 1119 (1987).

[36] V. Cherepanov, I. Kolokolov, and V. L'vov, The saga of YIG: spectra, thermodynamics, interaction and relaxation of magnons in a complex magnet, Phys. Rep. **229**, 81 (1993).

[37] W. Strauss, Magnetoelastic properties of yttrium-iron garnet, in *Physical Acoustics, Vol. IV-Part B: Principles and Methods, Applications to Quantum and Solid State Physics*, edited by W. P. Mason (Academic Press, New York, 1968).

[38] A. G. Gurevich and G. A. Melkov, *Magnetization Oscillations and Waves* (CRC Press, Boca Raton, FL, 1996).

[39] S. S. Shinozaki, Specific heat of yttrium iron garnet from 1.5 to 4.2 K, Phys. Rev. **122**, 388 (1961).

[40] A. Kamra, H. Keshtgar, P. Yan, and G. E. W. Bauer, Coherent elastic excitation of spin waves, Phys. Rev. B **91**, 104409 (2015).

[41] K. Shen and G. E. W. Bauer, Laser-induced spatiotemporal dynamics of magnetic films, Phys. Rev. Lett. **115**, 197201 (2015).

[42] Z. Qiu, K. Ando, K. Uchida, Y. Kajiwara, R. Takahashi, H. Nakayama, T. An, Y. Fujikawa, and E. Saitoh, Spin mixing conductance at a well-controlled platinum/yttrium iron garnet interface, Appl. Phys. Lett. **103**, 092404 (2013).

[43] N. Ogawa, W. Koshibae, A. J. Beekman, N. Nagaosa, M. Kubota, M. Kawasaki, and Y. Tokura, Photodrive of magnetic bubbles via magnetoelastic waves, Proc. Natl. Acad. Sci. U.S.A. **112**, 8977 (2015).

[44] C. Kittel, Interaction of spin waves and ultrasonic waves in ferromagnetic crystals, Phys. Rev. **110**, 836 (1958).

[45] A. Rückriegel, P. Kopietz, D. A. Bozhko, A. A. Serga, and B. Hillebrands, Magnetoelastic modes and lifetime of magnons in thin yttrium iron garnet films, Phys. Rev. B **89**, 184413 (2014).

[46] S. C. Guerreiro and S. M. Rezende, Magnon-phonon interconversion in a dynamically reconfigurable magnetic material, Phys. Rev. B **92**, 214437 (2015).

[47] J. H. P. Colpa, Diagonalization of the quadratic boson Hamiltonian, Physica A **93**, 327 (1978).

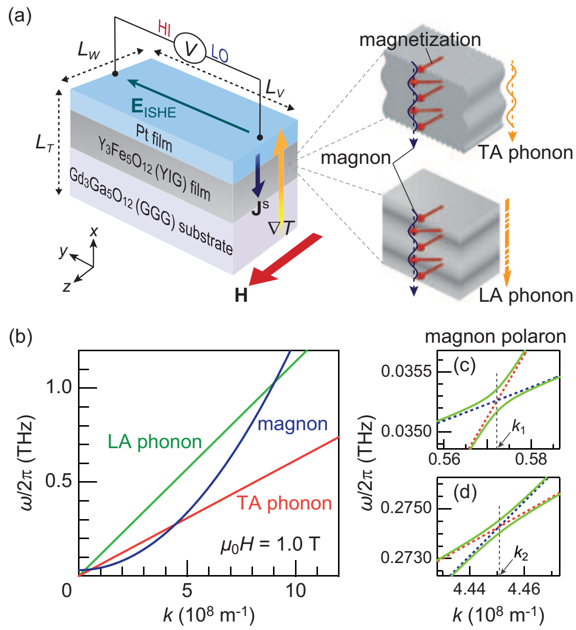

FIG. 1: (a) The longitudinal SSE in the Pt/YIG/GGG sample, where $\mathbf{E}_{\text{ISHE}}$ denotes the electric field induced by the ISHE. The closeup of the upper (lower) right shows a schematic illustration of a propagating magnon and TA (LA) phonon. (b) Magnon [Eq. (1) with $\mu_0 M_s = 0.2439$ T, $\mu_0 H = 1.0$ T, and $\theta = \pi/2$], TA-phonon ($\omega = c_\perp k$), and LA-phonon ($\omega = c_{||} k$) dispersion relations for the parameters in Table I. (c),(d) Magnon-polarons at the (anti) crossings between the magnon and TA-phonon branches at (c) lower and (d) higher wave numbers, where $\mathbf{k} \parallel \hat{\mathbf{x}}$ ($\theta = \pi/2$ and $\phi = 0$) and $\mathbf{H} \parallel \hat{\mathbf{z}}$.

TABLE I: Parameters for the magnon and phonon dispersion relations of YIG [34–39].

	Symbol	Value	Unit
Exchange stiffness	D_{ex}	7.7×10^{-6}	m^2/s
TA-phonon sound velocity	$c_\perp$	3.9×10^3	m/s
LA-phonon sound velocity	$c_{\|\|}$	7.2×10^3	m/s

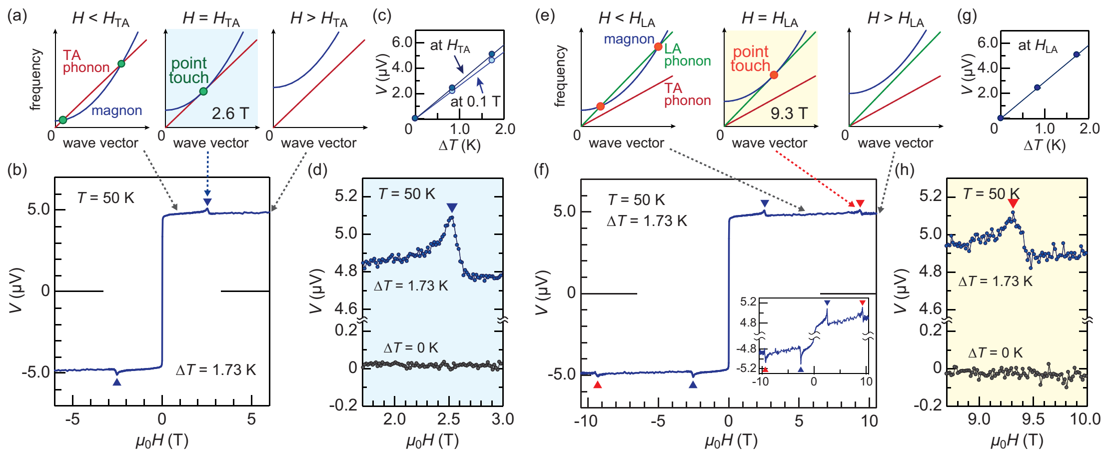

FIG. 2: (a) Magnon and TA-phonon dispersion relations for YIG when $H < H_{\mathrm{TA}}$, $H = H_{\mathrm{TA}}$, and $H > H_{\mathrm{TA}}$. (b) $V\,(H)$ of the Pt/YIG/GGG sample for $\Delta T = 1.73$ K at $T = 50$ K for $|\mu_0 H| < 6$ T. (c) $V\,(\Delta T)$ of the Pt/YIG/GGG sample at $\mu_0 H = 0.1$ T and $\mu_0 H_{\mathrm{TA}}$. (d) Magnified view of $V\,(H)$ around H_{TA}. (e) Magnon, TA-phonon, and LA-phonon dispersion relations for YIG when $H < H_{\mathrm{LA}}$, $H = H_{\mathrm{LA}}$, and $H > H_{\mathrm{LA}}$. (f) $V\,(H)$ of the Pt/YIG/GGG sample for $\Delta T = 1.73$ K at $T = 50$ K for $|\mu_0 H| < 10.5$ T. The inset to (f) is a magnified view of $V\,(H)$ for $4.6\ \mu\mathrm{V} < |V| < 5.3\ \mu\mathrm{V}$. (g) $V\,(\Delta T)$ of the Pt/YIG/GGG sample at $H = H_{\mathrm{LA}}$. (h) Magnified view of $V\,(H)$ around H_{LA}. The V peaks at H_{TA} and H_{LA} are marked by blue and red triangles, respectively.

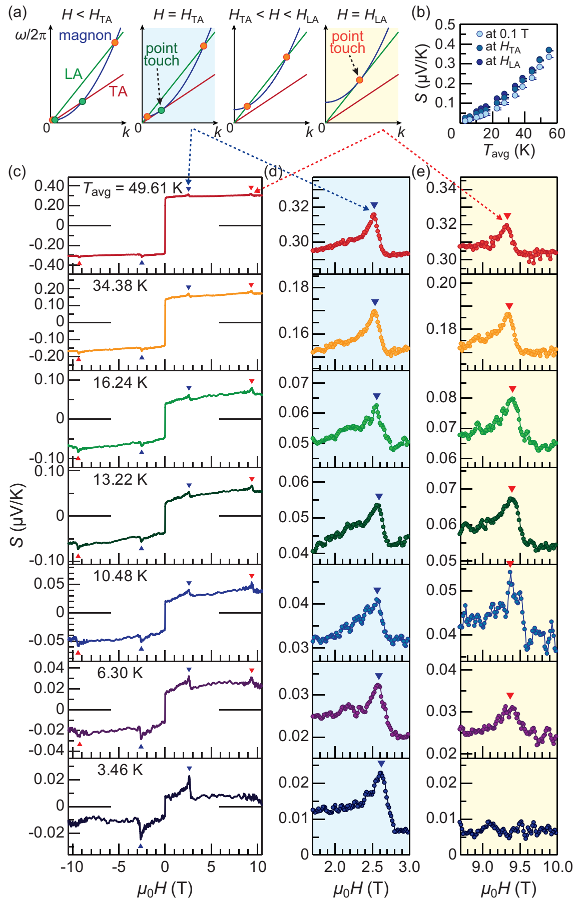

FIG. 3: (a) Magnon, TA-phonon, and LA-phonon dispersion relations for YIG when $H < H_{\rm TA}$, $H = H_{\rm TA}$, $H_{\rm TA} < H < H_{\rm LA}$, and $H = H_{\rm LA}$. (b) $T_{\rm avg}$ dependence of normalized SSE voltage S at $\mu_0 H = 0.1$ T, $\mu_0 H_{\rm TA}$, and $\mu_0 H_{\rm LA}$. (c) $S(H)$ of the Pt/YIG/GGG sample for various values of $T_{\rm avg}$ in the range of $|\mu_0 H| < 10.5$ T. (d),(e) A blow-up of $S(H)$ around (d) $H_{\rm TA}$ and (e) $H_{\rm LA}$.

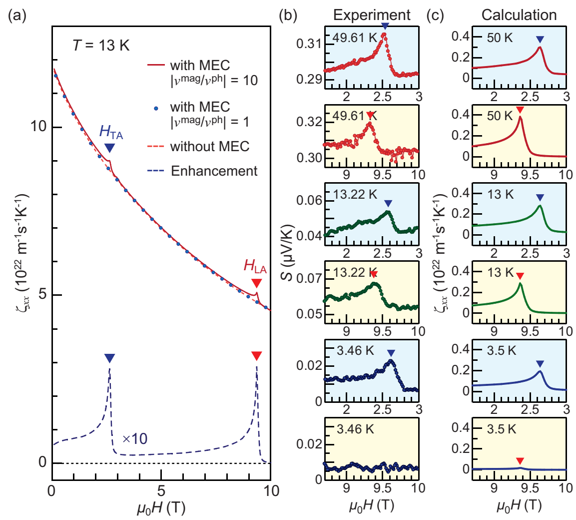

FIG. 4: (a) Calculated SSC ζ_{xx} at $T = 13$ K as a function of H, with (red solid curve and blue circles) and without (red dashed curve) magnetoelastic coupling (MEC). The red solid curve and the blue circles are computed for ratios of scattering potentials of $\left|v^{\mathrm{mag}}/v^{\mathrm{ph}}\right| = 10$ and $\left|v^{\mathrm{mag}}/v^{\mathrm{ph}}\right| = 1$, respectively. The blue dashed curve is a blow-up of the difference between the red curves. (b) Experimental S and (c) theoretical ζ_{xx} after subtraction of zero MEC results.